EXPERIMENTAL AND CFD OPTIMIZATION ON FLOW AND HEAT TRANSFER TO A SOLAR FLAT-PLATE GLASS COLLECTOR

Pascal Leibbrandt, Thomas Schabbach, Michael Dölz, Martin Rhein

Institut für Regenerative Energietechnik, University of Applied Sciences Nordhausen (Germany)

Abstract

In the project solar flat-plate glass collector, a new type of solar collector will be developed which, simplified, consists of four glass plates. As part of the project, the full volumetric flow in the fluid layer and the convective heat transfer in the insulating gas layer were investigated by using experimentally and numerically methods. Regarding to the fluid layer, an optimal fluid layer structure has been found which distributes the fluid well and ensures an optimal collector efficiency factor of nearly 99%. With the numerical simulation of the convective flow in the isolation gas layer it was shown, that the most used equation by Hollands (1976) presumably needs to be extended by the aspect ratio of the gas volume and other boundary conditions. These results are currently being validated experimentally. In addition, the filling/drainback process was examined for a potential drainback application.

Keywords: glass collector, fluid distribution, convective losses, CFD, validation

1. Collector construction and operation

In context of the research project "Nurglas-Solarflachkollektor" a collector with lower production costs is developed which consists primarily of glass. Due to the simplified construction, cost intensive production steps such as the absorber welding are unnecessary and enable an automated production process with fewer production steps. Manufacturing costs can thus be reduced by approximately 20% compared to conventional standard flat-plate collectors. Another advantage is the reduced collector thickness of < 40 mm which allows an simplified installation and collector field connection, so that other application areas (especially in facade) can be opened up.

The glass collector consists of four planar glass plates, which are glued and sealed by a frame and a fluid layer structure. As shown in Fig. 1, the heat transfer medium (yellow) passes directly through the middle rectangular space. The coatings on the glasses ensure optimal radiation absorption in the fluid layer and minimize the radiation losses due to reflection and emission, see also Leibbrandt et al. (2014). The heat transfer fluid has to be distributed full volumetric through the flow channel to ensure an optimal heat transfer coefficient h_{fl} in the fluid to optimize the collector efficiency factor. The fluid layer structure should also be able to absorb inner/outer forces from/to the fluid layer. Insulating gas layers (green) minimize convective heat losses to the front (h_{igf}) and back (h_{igb}).
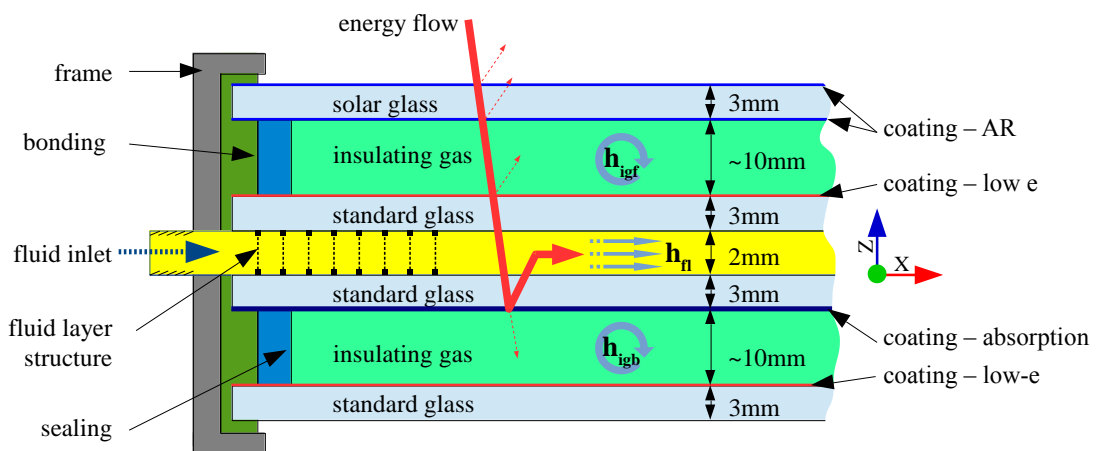

Fig. 1: Construction of the glass collector

2. Fluid layer: full volumetric flow and heat transfer

With an optimal collector efficiency factor F′, the overall collector efficiency is ensured. F′ is the theoretical ratio of the useful energy gain to the useful gain that would result if the absorbing surface would be at the fluid temperature, Duffie Beckman (2013). The collector efficiency factor is at its maximum if the flow would be full volumetric. For flat-plate collectors with a fin width of 90-120 mm, the collector efficiency factor is about 88-94%, Wesselak et al. (2017). The internal heat transfer U_{int} is at its maximum when the flow is fully homogeneous (without flow areas with no/low flow velocity) and turbulent. It is

$$F' = \frac{U_{int}}{U_{int} + U_{loss}} \qquad \text{(eq. 1)}$$

Fluid layer full volumetric flow

The flow channel with size L x B s_f = 2000 x 1000 2 mm should be flowed through full volumetric in the ideal case. In flow channels without internals, a flow like in Fig. 2 - A results. The flow field $\vec{u_i}$ consist of local velocity components in each direction. The ideal homogeneous velocity field (Fig. 2 - B) consists only of velocity components in x-direction and is equal in any position of the flow channel. It is

$$\textbf{A}: \vec{u_i} = \begin{pmatrix} u_i(x,y,z) \\ v_i(x,y,z) \\ w_i(x,y,z) \end{pmatrix} \qquad \textbf{B}: \vec{u_i} = \begin{pmatrix} u_i(x) \\ 0 \\ 0 \end{pmatrix} \qquad \text{(eq. 2)}$$
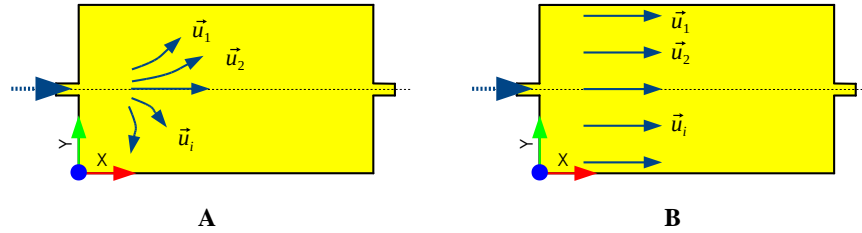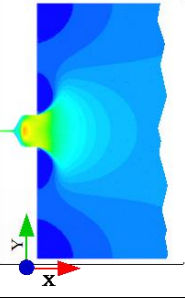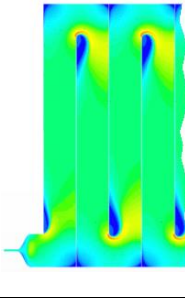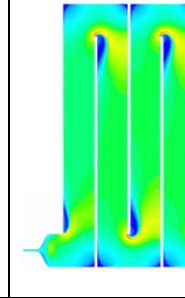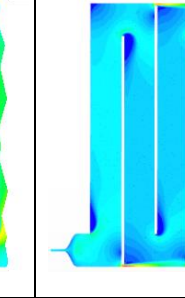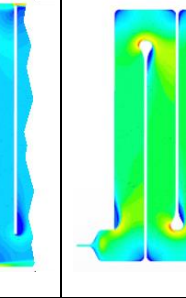

Fig. 2: Fluid Layer velocity fields

First 2D CFD simulations are able to model the flow in the fluid layer sufficiently precisely so that a further optimization of the fluid layer structure is carried out with CFD simulations. Results of the optimized version from a detailed 3D CFD model (flow channel 2000 x 1000 x 2 mm) with different fluid layer structure are illustrated in Tab. 1. The fluid layer structures with rectangular flow channels in meandering shape led to the best results in terms of flow distribution.

In addition to the local scalar velocities (row **1**) in the fluid layer (at z = 1 mm), the volume uniformity of the local velocities uni_u over the flow volume V was used to determine the homogeneity of the flow (row **2**). It is

$$uni_u = 1 - \frac{\sum_i |u_i - \bar{u}| \cdot V_i}{2|\bar{u}| \sum_i V_i} \qquad \text{(eq. 3)}$$

Tab. 1: Flow results for different fluid layer structures

	Structure 0 no inner web	Structure 1 web with narrow bars (1 mm)	Structure 2 web with wide bars (10 mm)	Structure 3 web with wide bars (10 mm) and end gaps	Structure 4 web with wide bars (10 mm) and end roundings
1					
2	$uni_u = 0.723$ m/s (reference)	$uni_u = 0.812$ m/s (+12,4%)	$uni_u = 0.817$ m/s (+13,0%)	$uni_u = 0.799$ m/s (+10,5%)	$uni_u = 0.823$ m/s (+13,9%)

An appropriate fluid layer structure, which distributes the heat transfer fluid almost full volumetric in the 2 mm fluid layer results of the detailed 3D CFD model. Experimental investigations of fluid layer prototypes confirm the simulation results and the flow behavior. In Fig. 3, an optical measurement of the flow field (left) is compared with 3D CFD results (right), see also Leibbrandt et al. (2017).
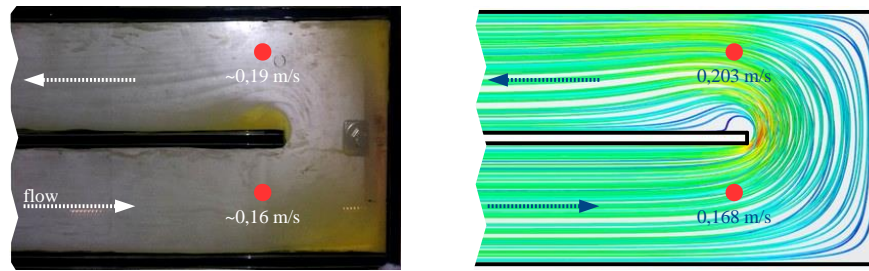

Fig. 3: Experimental and 3D CFD velocity field

At the same time the pressure drop and the filling/drainback performance is determined by experiments for a potentially drainback system application.

Fluid layer heat transfer

After the optimization of the fluid layer structure, the influence on heat transfer is investigated. The fluid layers' dimension is set to L x B x s_{fl} = 2000 x 1000 x 2 mm, the inclination of the layer is 45°.

For the simulations two fluid layer structures, similar to structure 0 and 2 are analyzed. The backside of the fluid channel is set up with a constant heat flow density $\dot{q}_{abs} = 700\ W/m^2$, which corresponds to the absorbed solar radiation power. At the front convective heat transfer with a constant heat transfer coefficient and fixed ambient temperature is assumed. In reality, the convective heat transfer coefficient depends on the front side temperature, too. The sides of the fluid channel have been supposed to be adiabatic. The fluid inlet temperature is 20 °C; the inlet velocity is varied between 0.25 – 1.00 m/s (35 – 140 l/(m² h)).

To rate the quality of the heat transfer coefficient h_{fl} through the fluid layer the useable enthalpy-flow $\dot{q}_{use}$ at the layer outlet is set into relation to mean fluid and absorber temperature difference. It is:

$$h_{fl} = \frac{\dot{q}_{use}}{\overline{T_{abs}} - \overline{T_{fl}}} \qquad\qquad (\text{eq. 4})$$

To compare the collector efficiency factor of the fluid layer F_f' with standard flat-plate collectors it is assumed, that the overall loss heat transfer coefficient is $U_{loss} = 4\,W/(m^2 K)$. U_{loss} describes the collector heat losses over the sides and the back of the collector which are not part of the presented CFD simulations. The efficiency factor of the fluid layer F_{fl}' is:

$$F_{fl}' = \frac{h_{fl}}{h_{fl} + U_{loss}} \qquad\qquad \text{(eq. 5)}$$

Tab. 1: Influence of fluid layer structures on heat transfer (3D CFD results)

		u_{in} in m/s		
		0.25	0.50	1.00
Structure 0	$\dot{q}_{use}$ in W/m²	565.95	630.53	657.35
	h_{fl} in W/m²/K	372.86	365.07	360.68
	$\boldsymbol{F_{fl}'}$	**98.9%**	**98.9%**	**98.9%**
Structure 2	$\dot{q}_{use}$ in W/m²	556.11	617.33	651.18
	h_{fl} in W/m²/K	343.25	421.14	625.53
	$\boldsymbol{F_{fl}'}$	**98.8%**	**99.1%**	**99.4%**

The useable enthalpy-flow $\dot{q}_{use}$ of structure 2 is less than in structure 0 because the heat loss to the front side is greater due to higher internal heat transfer and higher fluid temperatures.

Fig. 4 shows the temperature field inside the flow channels. A temperature inhomogeneity can be seen especially at the end of the individual fluid channels. They are formed due to the lower flow velocity and lead to local temperature maxima (hot spots). They should be minimized by a suitable flow guidance. At these hotspots the heat transfer reduces and high temperature gradients occur which also lead to stresses in the glasses.
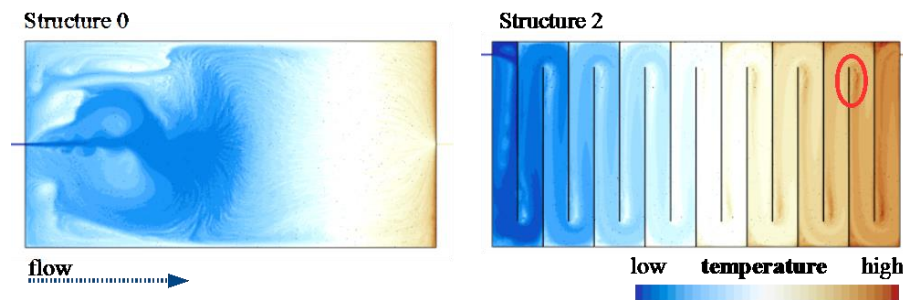

Fig. 4: Fluid Layer temperature fields (3D CFD results)

3. Insulating gas layer heat transfer

To ensure an optimal collector efficiency the convective front losses through the insulating gas layer is investigated. The gas volume, filled with insulating gas has a length L, a width B and a glass distance s, see Fig. 5. The resulting aspect ratio $AR = L/s$ is about 80 at standard flat-plate collectors (distance between absorber and front glass) and about 200 at the presented glass collector. The most used approach to calculate the convective heat transfer was investigated by Hollands et al. (1976).
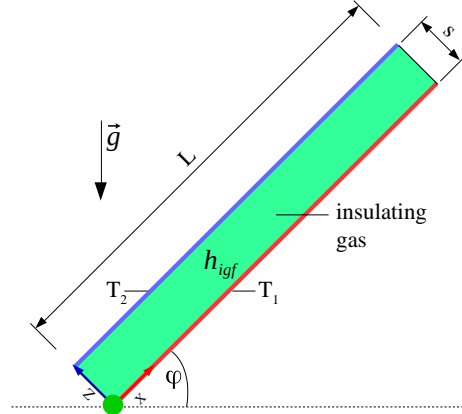

Fig. 5: Problem definition insulating gas layer

The internal heat transfer coefficient h_{igf} is at its minimum at the point where the gas flow velocity is low and the conductive isolating behavior of the gas is at its maximum.

The boundary conditions (e.g. temperature difference, homogeneity and level) and the geometric relationships (aspect ratio and vault of glasses) of the glass collector do not match those by Hollands et al. (1976). The deviations, when using the Hollands equation, for varying boundary condition were demonstrated, for example, by Föste (2013) by investigating an insulating glass flat-plate collector experimentally. Eismann (2014) showed the influence of the temperature inhomogeneity on the basis of collector simulations. The data in Tab. 2 show the wide range of geometry and boundary conditions. The error in calculating the heat transfer, as mentioned above, presumably results in these deviations.

Tab. 2: Geometry and boundary conditions

	Glass collector	Standard collector	Hollands et al. (1976)
Length L in mm	2,000	2,000	610
Glass distance s in mm	10	25	12.7
Aspect ratio AR	200	80	48
Insulating gas	argon	air	air
T_1 in C	70	120	26.67 (80 F)
T_2 in C	35	20	15.56 (60 F)
ΔT in K	35	100	11.1

The internal heat transfer is calculated with

$$\dot{Q} = A \cdot h_{igf} \cdot (T_1 - T_2).$$
(eq. 6)

The heat transfer coefficient h_{igf} is calculated from the Nusselt number Nu, which depends on the Rayleigh number Ra. The Rayleigh number describes the internal free convection.

$$Nu = Nu(Ra)$$
(eq. 7)

The Rayleigh number depends on the Grashof number Gr (ratio of lift forces and internal viscous friction forces) and the Prandtl number (material data).

$$Nu = \frac{h_{igf} \cdot s}{\lambda} \qquad \text{(eq. 8)}$$

$$Ra = Gr \cdot \Pr = \frac{g \cdot \beta \cdot \Delta T \cdot s^3}{\nu \cdot a} \qquad \text{(eq. 9)}$$

Hollands et al. (1976) developed the following Eq. from experimental measurement. The Eq. is split in three parts, depending on the Rayleigh number of the problem. The part $[...]^+$ activates the terms in brackets for different Rayleigh numbers.

$$Nu = 1 + 1.44 \left[1 - \frac{1708 \, (\sin(1.8 \cdot \varphi))^{\frac{1}{6}}}{Ra \cdot \cos(\varphi)} \right] \left[1 - \frac{1708}{Ra \cdot \cos(\varphi)} \right]^+ + \left[\left(\frac{Ra \cdot \cos(\varphi)}{5830} \right)^{\frac{1}{3}} - 1 \right]^+$$

Three different flow types, regarding to $Ra^* = Ra \cdot \cos(\varphi)$ are illustrated in Fig. 6. For $Ra^* < 1708$, the flow is quasi-conductive because the heat transfer media does move with very slow velocity. In the transition area $Ra^* = 1708 \dots \sim 5830$, the flow topology is characterized by a mono-cellular base flow. A multi-cellular flow regime arise for $Ra^* > 5830$. The optimal point of minimum heat transfer is at about $Ra^* \approx 1708$, where the isolating behavior of the gas is at its maximum.
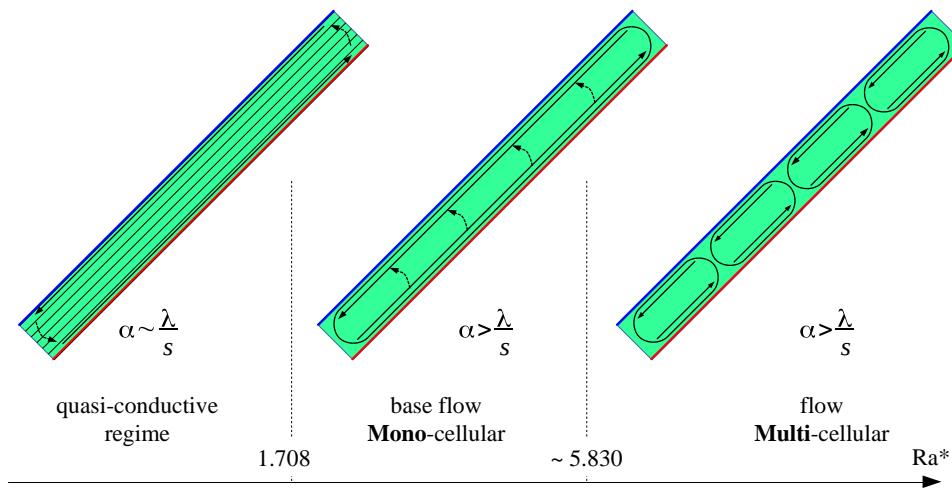

Fig. 6: Flow regimes

Based on intensive literature research, see Leibbrandt et al. (2016), the following conclusions for internal free convective flows in inclined cavities are known until now:

- Hollands et al. (1976) developed the correlation (see above) from experimental measurement and based on earlier theoretical research. The gas volume was captured between two nearly isothermal copper plates in a vacuum vessel. The change in Rayleigh number was set with varying pressure inside the vessel. So the aspect ratio AR was constant because of constant distance s. Also the humidity of the captured air was not documented, which led to an uncertainty in the heat transfer coefficient up to 6%. The correlation from Hollands et al. (1976) is based on an evaluation of the heat transfer in a central area (130 x 130 mm)of the copper plates. Later investigations show that the total heat transfer is significantly influenced by higher local heat transfer coefficients at the ends (top and bottom) of the gas volume, too.

- Bartelsen et al. (1993) and Föste (2013) showed that measured data from flat-plate collectors led to higher heat transfer coefficients about 10% regarding to Hollands et al. (1976). Measurements by Föste (2013) on isolating glass collector showed a deviation up to 32%. Yiqin et al. (1991) also investigated mean differences up to 10% in the heat transfer.

Insolating gas layer CFD simulation and validation

In this project, a CFD model is used to check the influence of varying boundary conditions and geometry. Numeric discretization and physics models are checked first in a simplified 2D CFD model and are validated with a 3D CFD model. Based on the experimental setup from Hollands et al. (1976) a detailed 3D CFD model calculates the internal flow and the heat transfer. The geometry, boundary conditions and report area (central) are the same as in Tab. 2 (Hollands). The Rayleih number is set with varying pressure from 70 Pa up to 700,000 Pa to capture the range of the setup from Hollands et al. (1976).

In Fig. 7 (left) the influence of varying discretization of the 3D CFD model is shown. For normal (cell size 1.0 mm) and coarse discretization (cell size 2.0 mm), the flow topologies and the heat transfer phenomena are captured unsatisfactory. Just the fine discretization (cell size 0.5 mm) is able to capture the behavior of the flow well. The discretization accuracy confirm the former 2D CFD results. An even finer discretization would lead to a disproportionate simulation time with no appreciable increase of the accuracy. Fig. 7 (right) shows the simulation results with two different flow models. The chosen one (LowRe: Reynolds-averaged Navier-Stokes model, coupled energy and flow with standard K-Epsilon Low-Re formulation) is able to model the flow well. The maximum deviation in h_{igf} is about 6.5% at 400,000 Pa.
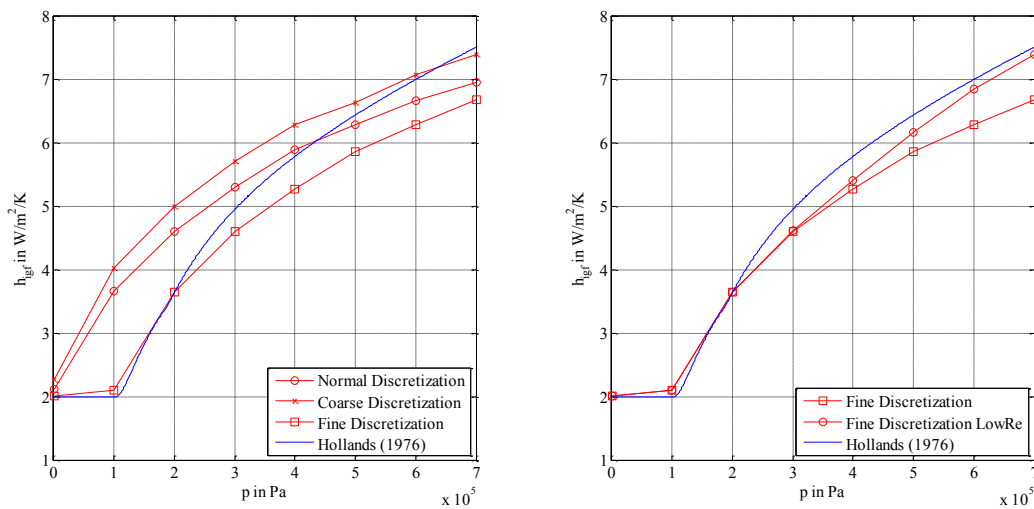

Fig. 7: Discretization influence (left) and flow model influence (right) of the 3D CFD model

Tab. 3 gives an overview of the different flow regimes. These results are scalar velocity- and temperature fields from a central section (bottom end) of the mentioned setup by Hollands et al. (1976) for fine discretization and LowRe flow model. The above-described flow regimes can clearly be seen in Tab. 3: for $p = 70\,Pa$ semiconductive behavior dominates, for p = 100,000 Pa a mono-cellular flow topology is visible, for Ra > 200,000 Pa turbulent multi-cellular flow cells are visible.

Tab. 3: Velocity- and temperature fields

p in Pa	Ra	Velocity field	Temperature field
70	0.001134		
100,000	2,313		
200,000	9,253		
300,000	20,820		
400,000	37,013		
500,000	57,832		
600,000	83,278		
700,000	113,351		

CFD simulation with varying boundary conditions

In the next step, the validated 3D CFD model is used to check the influence of heat transfer for varying geometry and boundary conditions. For this purpose all models and CFD setups are used, but for the first appraisal a 2D geometry is applied.

As mentioned above, the aspect ratio AR seems to have an influence on the flow regimes and so on the heat transfer phenomena. For this, simulations with varying $AR = 40 \ldots 200$ are presented in Fig. 8. It is obvious that the variation of AR results in an a difference of h_{igf} and Nu. Nu differs up to 11.6% for high Rayleigh numbers.
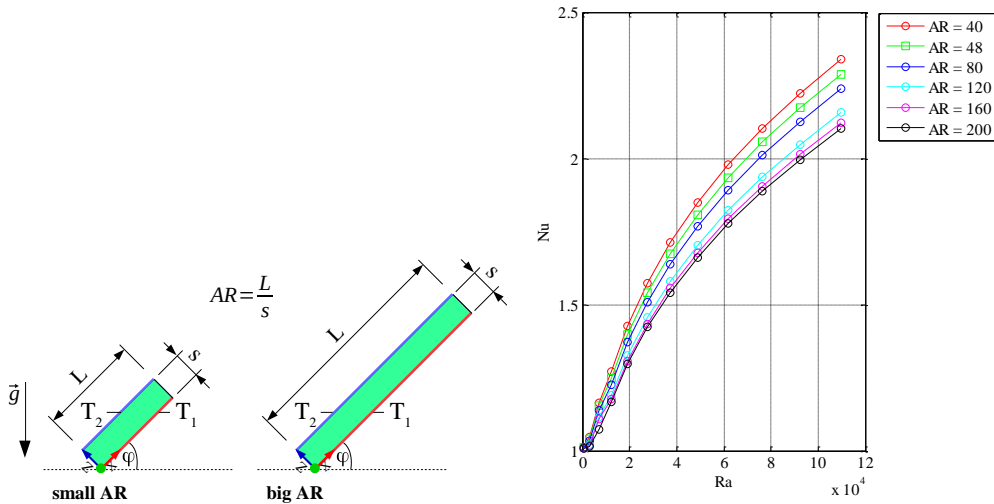

Fig. 8: Influence of varying AR (total area)

Another influence factor is the curvature of the glass plates. By default, the glass plates are considered as planar without any curvature. Due to varying temperatures while the collector operation, the resulting change in the density of the filling gas leads to a volume change of the gas and so to a curvature of the glasses. In the first step the glass planes are set to be parallel, so $s = const.$ and $ds = f(x)$, $ds(L/2)$ is varied with $ds_0 \ldots ds_2 = 0 \ldots 2 \ldots 4\ mm$. Results are presented for $AR = 20 \ldots 80$. For $AR = 20$, Nu differs up to 1.0% for $ds = 4\ mm$ and for $AR = 80$, Nu differs up to 0.7% for $ds = 4\ mm$, see Fig. 9.
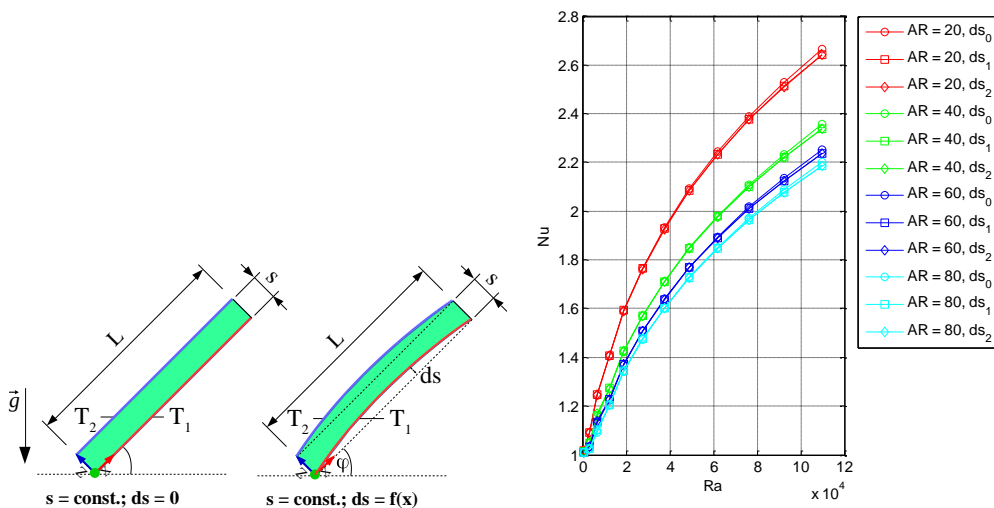

Fig. 9: Influence of varying ds (total area)

Last, the influence of a linear temperature profile $T_1 = f(x)$ is shown. In real collectors the fluid temperature increases over the collector length L due to the radiation absorption by a given flow direction. This effect is modeled by an linear temperature profile $T_1 = f(x)$, while the mean temperature $\overline{T}_1$ is constant. The influence of the linear temperature profile $dT/dL = 0 \ldots 2 \ldots 4\,K$ in Nu is maximum about 1.1% for $AR = 20$ and 0.5% for $AR = 80$.
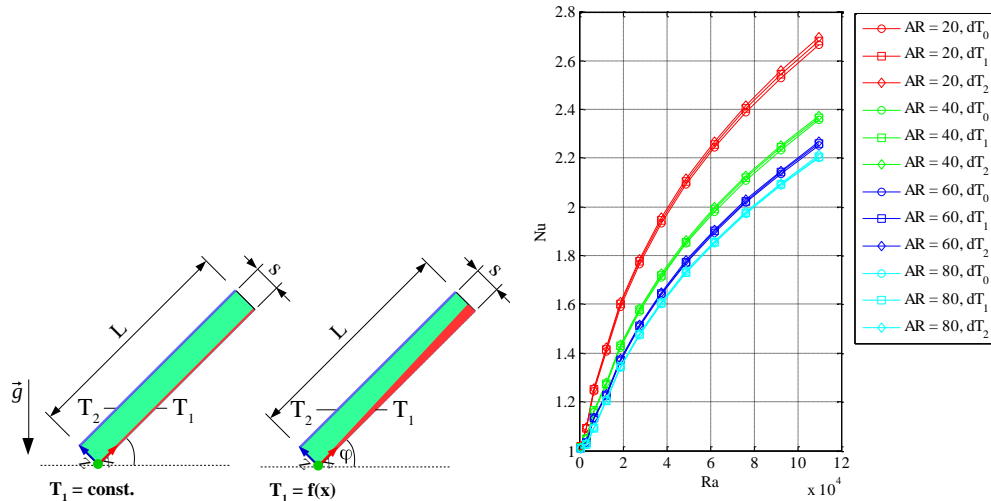

Fig. 10: Influence of varying T₁ (total area)

With CFD simulations, it is shown that the heat transfer coefficient h_{igf} depends on the boundary conditions mentioned above. This results for different AR in variation of h_{igf} up to 11.6%. The influence of AR is not component of the equation by Hollands et al. (1976), so that an extension of that equation should be carried out. For inhomogeneous temperatures and vaulted gas volumes, the influence is lower but not negligible.

Experimental investigations

To validate the simulation results, an experimental setup is under construction at the moment. A heating mat generates a one dimensional heat flux $\dot{q}(x, y)$ field, which is determined by a measurement layer and allows to measure the heat transfer trough the insulating gas layer. With temperature sensors, a spatially resolved heat flux field is used to calculate a spatially resolved heat transfer coefficient field $h_{igf}(x, y)$. The measurements are used to validate the simulation results and should allow to extend the present calculation approaches.

4. Outlook

In continuation to the project collector prototypes will be investigated experimentally. Target will be to increase the flow homogeneity, heat transfer and stability of the fluid layer. The pressure loss, manufacturability and long term stability must also be considered. The performance of the entire collector will be checked during QDT-testing. Mechanical load tests with internal and external forces will also take place.

5. Acknowledgement

6. References

Bartelsen et al. 1993. Heat Transfer by Natural Convection in the Air Gap of Flat Plate Collectors. Proceedings ISES Solar World Congress, pp. 267-273, Budapest

Dölz; Schabbach; Leibbrandt; Rhein, 2016. Low-Cost-Kollektorprüfstand für quasidynamische Messungen im Hochtemperaturbereich. 26. OTTI Symposium Thermische Solarenergie, Bad Staffelstein

Duffie, Beckman, 2013. Solar Engineering of Thermal Processes, fourth ed. John Wiley & Sons Inc., Hoboken, New Jersey

Eismann, R. 2014. Thermohydraulik von Solaranlagen. ETH Zürich, Dissertation

Föste, S. 2013. Flachkollektor mit selektiv beschichteter Zweischeibenverglasung. Gottfried Wilhelm Leibniz Universität Hannover, Dissertation

Hollands et al. 1976. Free Convective Heat Transfer Across Inclined Air Layers. J. Heat Transfer 98(2), 189-193

Leibbrandt; Schabbach; Weber, 2014. Flachkollektoren aus Glas – erste Untersuchungsergebnisse. 24. OTTI Symposium Thermische Solarenergie, Bad Staffelstein

Leibbrandt; Schabbach; Dölz; Rhein, 2016. CFD-Untersuchungen zu konvektiven Wärmeverlusten in Scheibenzwischenräumen mit großem Seitenverhältnis. 26. OTTI Symposium Thermische Solarenergie, Bad Staffelstein

Leibbrandt; Schabbach; Dölz; Rhein, 2017. Experimentelle und numerische Untersuchungen zur vollvolumetrischen Durchströmung von Isolierglaskollektoren. 27. OTTI Symposium Thermische Solarenergie, Bad Staffelstein

Rhein; Schabbach; Dölz; Leibbrandt, 2016. Strukturanalyse eines Nurglaskollektors unter Berücksichtigung statischer und dynamischer Lasten. 26. OTTI Symposium Thermische Solarenergie, Bad Staffelstein

Wesselak et al. 2017. Regenerative Energietechnik, 3. ed. Springer Vieweg, Berin, Heidelberg

Yiqin et al. 1991. Measured Top Heat Loss Coefficients for Flat Plate Collectors with Inner Teflon Covers. Proceedings of the Biennial Congress of the International Solar Energy Society, Denver, Colorado